Second Harmonic Generation

4.1 Foundations of Nonlinear Optics

Maxwell's equations, on a classical microscopic level, capture the dynamics of all free and bound charges [133]. However, because the electric field varies extremely rapidly over atomic length scales, the microscopic description loses relevance when considering macroscopic problems, such as the interaction of light with matter. The bound charges in matter react to external electrical fields by rapidly rearranging, resulting in a polarization field produced in response to the applied field. Because the bound charges' motion are constrained by their neighboring electrons and protons, which are also moving, the material response is extremely complex in microscopic detail. Fortunately, it tends to be characteristic of the material in question. In practice,

this is addressed by averaging out the variations over atomic length scales, producing the macroscopic Maxwell's equations:

$$\nabla \cdot \mathbf{D} = \rho_f \tag{4.1a}$$

$$\nabla \cdot \mathbf{B} = 0 \tag{4.1b}$$

$$\nabla \times \mathbf{E} = -\frac{\partial \mathbf{B}}{\partial t} \tag{4.1c}$$

$$\nabla \times \mathbf{H} = \mathbf{J}_f + \frac{1}{c^2}\frac{\partial \mathbf{D}}{\partial t}, \tag{4.1d}$$

where $\mathbf{D} = \epsilon_0 \mathbf{E} + \mathbf{P}$ is the displacement field, **E** is the native field due to free charges or applied external fields, **P** is the polarization field created by matter responding to **E**. The magnetic field due to **E** and induced magnetization of the material due to **H** play a minimal role in this work, and the reader is referred to excellent texts such as Jackson [133] for further exploration, but we will confine ourselves to the case where $\mathbf{B} = \mu_0 \mathbf{H}$. Furthermore, this work is concerned only with how bound charges respond to externally applied fields, so we take $\rho_f = 0$ and $\mathbf{J}_f = 0$.

The wave-equation is constructed by taking the curl of eq. (4.1c) and substituting into equation 4.1d. The resulting equation, $\nabla \times \nabla \times \mathbf{E} + \frac{\partial \mathbf{D}}{\partial t} = 0$, is converting into the wave equation by employing the vector identity $\nabla \times \nabla \times \mathbf{E} = \nabla(\nabla \cdot \mathbf{E}) - \nabla^2 \mathbf{E}$, and taking $|\nabla(\nabla \cdot \mathbf{E})| \ll |\nabla^2 \mathbf{E}|$ [113]:

$$\frac{1}{}\frac{\partial^2 \mathbf{E}}{} \quad \frac{1}{}\frac{\partial^2 \mathbf{P}}{}$$

$$\nabla \mathbf{E} - = \frac{\partial^2}{c^2 \partial t^2} \quad \frac{\partial^2}{c^2 \partial t^2} \tag{4.2}$$

The polarization, **P**, is due to the response of the underlying matter to the applied external field, **E**, which may be expanded as

$$\mathbf{P}(t)/\epsilon_0 = \mathbf{P}_0 + \int_{-\infty}^{\infty} \chi^{(1)}(\omega', \omega_1) : \mathbf{E}(\omega_1) e^{-i\omega' t}\, d\omega_1$$

$$+ \int\int_{-\infty}^{\infty} \chi^{(2)}(\omega', \omega_1, \omega_2) : \mathbf{E}(\omega_1)\mathbf{E}(\omega_2) e^{-i\omega_0 t}\, d\omega_1 d\omega_2 + \cdots$$

$$+ \cdots \int\int_{-\infty}^{\infty} \chi^{(n)}(\omega', \omega_1, \ldots, \omega_n) : \mathbf{E}(\omega_1)\cdots\mathbf{E}(\omega_2) e^{-i\omega_0 t} \prod_i d\omega_i \ldots, \tag{4.3}$$

where the colon indicates a tensor product and $\mathbf{P}_0$ is the static polarization, often found at surfaces or in ferroelectrics, and $\omega^0 = \omega_1 + \cdots + \omega_n$, where n is the order of the term in the expansion. This is often written with the shorthand notation $\mathbf{P}(\mathbf{E}) = \epsilon_0\{\mathbf{P}_0 + \chi^{(1)}\mathbf{E} + \chi^{(2)}\mathbf{E}^2 + \ldots\}$.[1] Because polarizability also acts as a source of electric field, see eq. (4.2), we expand the frequency components of the electric field in orders, $\mathbf{E}(\omega) = \mathbf{E}^{(1)}(\omega) + \mathbf{E}^{(2)}(\omega) + \ldots$, where each order is the contribution of the n^{th}-order nonlinear process. Thus, each order of nonlinearity has a corresponding wave

[1] Although this power series expansion is formally correct, it is only meaningful when it can be truncated. For this to be true, the terms must rapidly vanish, and this may not be the case under some conditions, such as in laser-induced breakdown ionization [125] or even under intense near-field optics [113]. The maximum peak intensity of the incoming field correspond to to electron binding energies, $I_{atom} \sim \frac{ce}{\epsilon_0 a_0^2} \sim 10^{15}$ W/cm^2. Once the incoming laser intensities reach this order of magnitude, perturbative expansions do not capture the full flavor of the nonlinear processes.

equation. Assuming negligible conversion from higher order modes to lower order modes,[2] the n[th]-order wave equation is given by

$$\nabla^2 \mathbf{E}^{(n)}(\omega) - \frac{1}{c^2}\frac{\partial^2}{\partial t^2}\mathbf{E}^{(n)}(\omega) = \frac{1}{c^2}\frac{\partial^2}{\partial t^2}\chi^{(1)}(\omega)\mathbf{E}^{(n)}(\omega) + \frac{1}{c^2}\frac{\partial^2}{\partial t^2}\chi^{(n)}(\omega)\mathbf{E}(\omega_1)\mathbf{E}(\omega_2)\dots$$
$$\nabla^2 \mathbf{E}^{(n)}(\omega) - \frac{n_\omega^2}{c^2}\frac{\partial^2}{\partial t^2}\mathbf{E}^{(n)}(\omega) = \frac{1}{c^2}\frac{\partial^2}{\partial t^2}\chi^{(n)}(\omega)\mathbf{E}(\omega_1)\mathbf{E}(\omega_2)\dots, \tag{4.4}$$

where n_ω^2 is the squared index of refraction, coming from $n_\omega^2 = \mu_r(1+\chi^{(1)}(\omega))$ and μ_r = 1. The susceptibility's dependence on incoming frequencies has been suppressed for convenience. When the incoming radiation consists of a single monochromatic plane wave, $\mathbf{E} \propto \cos(\omega t - kx)$, we can see that the n[th]-order nonlinearity will mix the positive and negative frequency components together to produce output frequencies that are both higher and lower than the fundamental. For example, in the second-order case, $P^{(2)} \propto \frac{1}{2}(\cos(2\omega t - 2kx) + 1)$, so there will be induced second harmonic generation and an optically induced dc field (optical rectification). When the two incoming fields are different frequencies, in addition to SHG and optical rectification, there will be sum frequency generation ($\omega^0 = \omega_1 + \omega_2$) and difference frequency generation ($\omega^0 = \omega_1 - \omega_2$). At higher orders, even more combinations are possible, leading to an entire catalog of possible nonlinear optical effects [134].

[2] This is true within the scope of the present work, but not in general.

Returning to the example of second harmonic generation from monochromatic plane waves, the second-order nonlinear wave equation becomes

$$\nabla^2 \mathbf{E}^{(n)}(\omega) - \frac{n_\omega^2}{c^2}\frac{\partial^2 \mathbf{E}^{(n)}(\omega)}{\partial t^2} + cc = -\frac{2\omega_1^2}{c^2}\chi^{(2)} E_0^2 e^{-2i(\omega_1 t - k_\omega x)} + cc, \tag{4.5}$$

where *cc* stands for the complex conjugate of the preceding terms. Because of the linearity of the equation, we have $\omega = 2\omega_1$, and a solution of the form $E(2\omega_1,x) = A(x)e^{-i(2\omega_1 t - k_{2\omega_1} x)} + cc$. This leads to

$$\frac{\partial^2}{\partial x^2}A(x) - ik_{2\omega_1}\frac{\partial}{\partial x}A(x) + cc = -\frac{2\omega_1^2}{c^2}\chi^{(2)} E_0^2 e^{i\Delta k x} + cc, \tag{4.6}$$

where $\Delta k = 2k_{\omega_1} - k_{2\omega_1} = 2\omega(n_{\omega_1} - n_{2\omega_1})/c$. Δk is the deviation from perfect phasematching. When $\Delta k \neq 0$, the fundamental and harmonic waves do not travel at the same speed, so the harmonic waves being to interfere with themselves. Taking $A(0) = \partial_x A(0) = 0$, meaning $A(x)$ represents the amplitude of the SHG produced after the fundamental mode is incident on a uniform slab of SHG-producing material, eq. (4.6) has a solution given by

$$A(x) = \frac{2\omega_1^2}{c^2}\chi^{(2)} E_0^2 \frac{k_{2\omega_1}(1 - e^{i\Delta k x}) - \Delta k(1 - e^{-ik_{2\omega_1} x})}{\Delta k k_{2\omega_1}(\Delta k + k_{2\omega_1})}.$$

The intensity of the resulting SHG is given by $n_{2\omega_1}(\epsilon_0/\mu_0)^{\frac{1}{2}}|A(x)|^2/2$, so, assuming $\Delta k \ll k_{2\omega_1}$, we obtain [134, 113]

$$I_{2\omega_1}(x) = \frac{\omega_1^2}{4c^3\epsilon_0}\frac{|\chi^{(2)}(\omega_1)|^2}{n_{\omega_1}^2 n_{2\omega_1}} I_{\omega_1}^2\, x^2 \mathrm{sinc}^2(\Delta k x/2), \tag{4.7}$$

where sinc is $\sin(x)/x$. This relationship illustrates the importance of phase-matching in creating SHG. As shown in figure 4.1, the size of the underlying SHG-active material makes a significant contribution to the overall SHG production efficiency.[3] However,

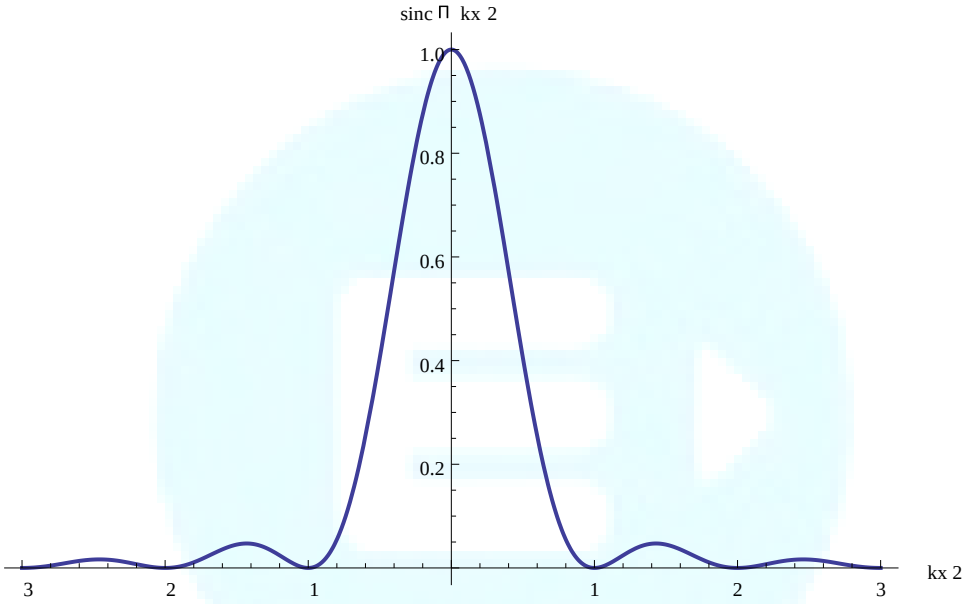

Figure 4.1: Second harmonic generation production efficiency depends on the magnitude of the phase-matching, Δk, determined by eq. (4.7). Absent perfect phasematching, corresponding to $\Delta k = 0$, SHG can only be produced across a distance constrained by $\Delta k \Delta x < 2\pi$.

[3] We recover the interesting relationship that SHG production is only significant when $x\Delta k < \pi$,

eq. (4.7) only holds for monochromatic plane waves. In practice, our experiments employ focused beams, which can significantly alter the phase-matching relations, and this will be more thoroughly explored in Section 4.2.

4.2 SHG Phase-Matching with Focused Light

Muscle fibers are significantly larger than the wavelength of light, as shown in figure 3.7, and the myofibrils are on order one wavelength. From eq. (4.7), only media much smaller than the wavelength of light escape the effects of phase-matching.

---

an analogy to the Heisenberg uncertainty principle, $\Delta x \Delta p > \sim/2$, although the current result originates from harmonic analysis. Given this analogy, we can explore the concept that SHG production is limited by the conservation of momentum mismatch resulting from the fusion of two photons into one. In the absence of perfect phase-matching, the outgoing photon will not conserve momentum. However, over very short distances, there is sufficient uncertainty in momentum to compensate for this. In addition, conceptually, vibrational quanta created by periodic order in the material can contribute or withdraw momentum to assist with momentum conservation.

However, focused light has a Guoy phase, an extra twist of phase that occurs at the focus [113]. In addition, focused light approaches the focus from different angles, giving more possible combinations for phase-matching. These effects can significantly alter the total phase-matching balance, a crucial factor to include in any theory of wavelength dependent SHG microscopy.

The susceptibility tensor for myosin, $\chi^{(2)}_{ijk}$, has a number of restrictions due to the underlying symmetry of the protein structures [129], leaving only two independent terms, $\chi_{(2)xxy} = \chi_{(2)xyx} = \chi_{(2)zyz} = \chi_{(2)zzy} = \chi_{yzz(2)} = \chi_{yxx(2)}$ and $\chi_{(2)yyy}$. Experiments have determined $\chi^{(2)}_{yyy} < \chi^{(2)}_{yxx}$. However, we leave analyses of the tensor components to

previous works [121, 106, 101, 129, 86]. In general, we will not need to consider the tensor nature of SHG, because the area of interest, the laser focus, is so small. In addition, we have chosen the alignment of the fish with the laser to be such that the SHG power is large. Taking the myosin to run along the *y*-axis, we set the polarization to be approximately perpendicular to y. Because the light is propagating in the *z*direction, and therefore has minimal vector components in z, we have essentially set up the experiment to probe a single tensor component, $\chi^{(2)}_{yxx}$.

4.2.1 The Paraxial Approximation of the Wave Equation

Consider the wave equation, $(\nabla^2 - \frac{n^2}{c^2}\partial_t^2)\mathbf{E} = 0$. The electric field is fundamentally a vector, which evolves in magnitude and orientation over space and time. Represent the electric field propagating in the $\hat{k}$ direction as $\mathbf{E}(\mathbf{r}) = \mathbf{A}(\mathbf{r})\exp(-i\omega t + i\mathbf{k}\cdot r)$. After decomposing the Laplacian into a transverse component and a radial component, $\nabla^2 = \nabla^2_{\hat{k}} + \nabla^2_T$, we substitute both expressions into the wave equation, obtaining the quantity

$$\nabla^2\mathbf{A}(\mathbf{r})\exp(i\mathbf{k}\cdot\mathbf{r}) = \exp(i\mathbf{k}\cdot\mathbf{r})\left(\nabla^2_T\mathbf{A}(\mathbf{r}) + 2i\mathbf{k}\cdot\mathbf{r}\,\nabla_{\hat{k}}\mathbf{A}(\mathbf{r}) + \nabla^2_{\hat{k}}\mathbf{A}(\mathbf{r})\right).$$

If $|\mathbf{k}\cdot\mathbf{r}\,\nabla_{\hat{k}}\mathbf{A}(\mathbf{r})| \gg |\nabla^2_{\hat{k}}\mathbf{A}(\mathbf{r})|$, meaning the envelope of the electric field varies slowly over the scale of a wavelength in the direction of propagation, the second-order term may be neglected, which is called the paraxial approximation [133]. This approximation is well suited for focused light, but it begins to break down when the

NA exceeds approximately 1 [135, 136, 137]. Although, the paraxial approximation has been shown to be lacking in accuracy for the angular radiation pattern of SHG [135], it has performed well for predicting the total power produced [138, 139, 140].

Given the paraxial approximation, one may describe a focused laser, propagating in the *z*-axis, using a Gaussian envelope,

$$A(r,z) = \frac{A_0}{1+i\xi}\exp\left[-\frac{r^2}{w_0^2(1+i\xi)}\right], \tag{4.8}$$

where we have adopted the notation of [113], and we define $\xi = 2z/b$, where b is the confocal parameter, $b = kw_0^2$, and w_0 is the radius of the beam at the focus. The nonlinear wave equation for SHG under the paraxial approximation gives

$$2ik_2\frac{\partial A_2}{\partial z} + \nabla_T^2 A_2 = -2\pi\frac{\omega^2}{c^2}\chi^{(2)}A(r,z)e^{-i\Delta kz}, \tag{4.9}$$

where ω is the fundamental frequency, A_2 is the resulting SHG mode, k_2 is the wavenumber at 2ω, $k_2 = 2n_{2\omega}\omega/c$, and the phase mismatch is $\Delta k = 2\frac{\omega}{c}(n_\omega - n_{2\omega})$. The solution to eq. (4.9) is given by

$$A_2(r,z) = i\frac{2\omega}{n_{2\omega}c}\chi^{(2)}A_0^2 J_2(\Delta k, z_0, z)\frac{\exp\left[-2\frac{r^2}{w_0^2(1+i\xi)}\right]}{1+i\xi}, \tag{4.10}$$

where

$$J_2(\Delta k, z_0, z_f) = \int_{z_0}^{z_f}\frac{e^{i\Delta kz'}}{1+2iz'/b}\,dz', \tag{4.11}$$

where z_0 is the z-coordinate of the beginning of the SHG medium, relative to the focus at $z = 0$ [113, 141]. This integral, which reduces to the identical form of eq. (4.7) when $z_0 - z_f \ll b$, determines the altered phase-matching conditions of the focused beam. As the limits of the integral in eq. (4.11) expand to infinity, J_2 takes the asymptotic form $J_2 = \{0, \Delta k \leq 0; \frac{b}{2}\exp(-b\Delta k/2), \Delta k > 0\}$ [113]. Even when the bounds are well short of the asymptotic limit, the integral is very sensitive to Δk and to the width of the medium, shown in figure 4.2.

4.2.2 SHG from Periodic Media

Derivations such as eq. (4.8) assign no explicit spatial dependence to the SHG susceptible medium. Most crystals are uniform at super-atomic lengths, but muscles, as described in section 3.1, are packed into multiscale structures, interleaving SHG and nonSHG active regions. Hence, it would be most appropriate to describe the

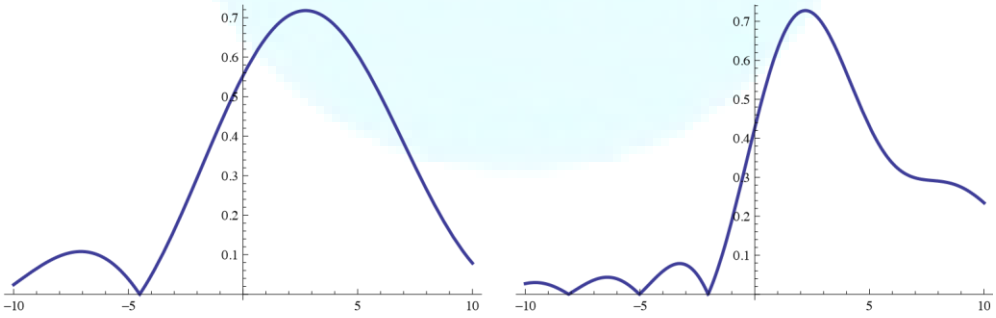

(a) $|J_2(\Delta k)|,\ z_f - z_0 = 1.$ (b) $|J_2(\Delta k)|,\ z_f - z_0 = 2.$

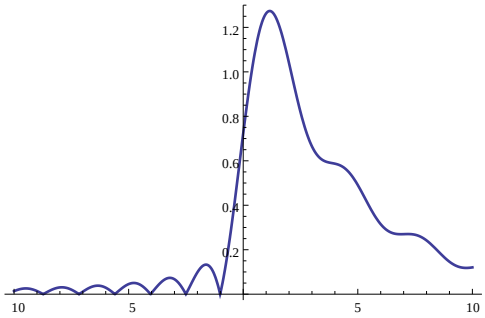

(c) $|J_2(\Delta k)|, z_f - z_0 = 4$.

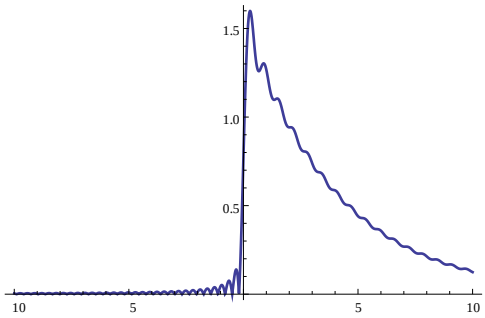

(d) $|J_2(\Delta k)|, z_f - z_0 = 20$.

Figure 4.2: With a focused beam, the conversion efficiency is very sensitive to the magnitude and sign of the phase-matching, Δk, as well as the width of the medium, $z_f - z_0$. $b = 0.5$

susceptibility with some sort of spatial regularity, i.e., $\chi^{(2)}(r)$.[4] We insert $\chi^{(2)}(\mathbf{r})$ into the nonlinear wave equation and expand in a Fourier series:

$$\begin{aligned}\nabla^2 A_2 - \frac{n_{2\omega}^2}{c^2}\frac{\partial^2}{\partial t^2}A_2 &= -2\pi\frac{\omega^2}{c^2}A^2(r,z)\chi^{(2)}(r)e^{-i\Delta kz} \\ &= -2\pi\frac{\omega^2}{c^2}A^2(r,z)\chi_0^{(2)}\sum_{lmn}G_{lmn}e^{-i(\Delta k+K_{lmn})\cdot\mathbf{r}},\end{aligned} \tag{4.12}$$

where $\mathbf{K}_{lmn}$ are the reciprocal lattice vectors of the SHG photonic crystal, G_{lmn} is the complex amplitude of each Fourier component, and l,m,and n are integers [142]. eq. (4.12) demonstrates that periodicity alters the phase-matching relationship into $\Delta\mathbf{k}^0 = \Delta\mathbf{k} + \mathbf{K}_{lmn}$. The resulting quasi-phase-matching allows multiple radiation directions, for each solution of

[4] Muscle is not merely periodic in its SHG susceptibility, but protein has a different index of refraction than water. Thus, there is a second spatial component, $n_{2\omega} = {}^{\mathrm{P}}N_{lmn}\exp(-\mathbf{K}_{lmn}\cdot\mathbf{r})$, which has identical lattice vectors. However, the difference in refractive index is small, while the difference in SHG susceptibility is large, so we may neglect the former.

$$\mathbf{k}_2 = 2\mathbf{k}_1 - \mathbf{K}_{lmn}, \tag{4.13}$$

which is consistent with the model that the periodic structure can add or subtract phonons to conserve momentum [143, 144]. The resulting angle will be given by

$$\cos\theta_{lmn} = 2\frac{k_1}{k_2} + \frac{\hat{k}_1 \cdot \mathbf{K}_{lmn}}{k_2} \tag{4.14}$$

$$= \frac{n_\omega}{n_{2\omega}} + \frac{\lambda}{2n_{2\omega}a}\hat{k}_1 \cdot \mathbf{K}'_{lmn}, \tag{4.15}$$

where θ_{mn} is the angle formed between k_1 and k_2, $\hat{k}_1$ is the unit vector oriented in the direction of propagation of the fundamental wave, and a is the characteristic length scale of the periodic structure.

For example, in a 2D-hexagonal crystal of circular rods, which has only two indices, m and n, the lattice is defined by two vectors, $(0,a)$ and $(\sqrt{3}a/2, a/2)$, where a is the spacing between neighboring elements. These two vectors form a parallelogram outlining the unit cell, shown in figure 3.6, and have the Fourier components given by [145]:

$$G_{mn} = \frac{2r}{a\sqrt{m^2+n^2+mn}} J_1\left(\frac{4\pi r}{\sqrt{3}a}\sqrt{m^2+n^2+mn}\right), \text{ and} \tag{4.16}$$

$$\mathbf{K}^{mn} = \frac{2\pi}{a}\left(\frac{1}{\sqrt{3}}(m+2n), m\right), \tag{4.17}$$

where r is the radius of the circular rod and J_1 is the first Bessel function. Assuming the laser enters the crystal at an angle φ, so $\hat{k}_1 = (\cos\varphi, \sin\varphi)$, eq. (4.14) becomes

$$\cos\theta_{mn} = \frac{n_\omega}{n_{2\omega}} + \frac{\lambda}{2n_{2\omega}a}\left(m\cos\phi + \frac{1}{\sqrt{3}}(m+2n)\sin\phi\right). \tag{4.18}$$

Sometimes no phase-matching conditions are readily apparent. However, it may be the case that phase-matching may be obtained by the outgoing SHG having a angular distribution that cannot be readily derived by the paraxial approximation. To account for this, and to study nontrivial geometries, we turn to a Green's function approach to calculating SHG. Because the nonlinear polarization acts as a source term in the wave equation, we sum the contribution from each point in the SHG medium [146]

$$\mathbf{E}_{2\omega}(\mathbf{r}) = \int G(\mathbf{r},\mathbf{r}^0)\mathbf{P}_{NL}(\mathbf{r}^0)d\mathbf{r}^0 \tag{4.19}$$

$$= \int G(\mathbf{r},\mathbf{r}')\sum_{jk}\chi^{(2)}_{ijk}(\mathbf{r}')E_j(\mathbf{r}')E_k(\mathbf{r}')\,d\mathbf{r}', \tag{4.20}$$

where $G(\mathbf{r},\mathbf{r}^0)$ is the Green's function, which, technically, depends on the specific boundary conditions. Although this is a very general expression, we are only really concerned about radiation in the far field, and, because only light collected by the condenser reaches the detector, we are concerned with the angular dependence of the radiation intensity. This simplifies the expression of the Green's function to be

approximately independent of near-field boundary conditions [133], and eq. (4.20) at a far-field distance R becomes [147, 140]

$$\mathbf{E}_{2\omega}(\Omega, \mathbf{r}_0) = \left[\hat{\theta}, \hat{\phi}\right] \cdot \frac{\omega^2}{c^2} \frac{e^{ik_{2\omega}R}}{4\pi R} \sum_{jk} \int \chi^{(2)}(\mathbf{r}') E_j(\mathbf{r}' - \mathbf{r}_0) E_k(\mathbf{r}' - \mathbf{r}_0) e^{-ik_{2\omega}\mathbf{r}'\cdot\hat{\mathbf{r}}}\, d\mathbf{r}', \quad (4.21)$$

where the spherical unit vectors are given by

$$\hat{\theta} = \cos\theta \cos\varphi \hat{\mathbf{x}} + \cos\theta \sin\varphi \hat{\mathbf{y}} - \sin\theta \hat{\mathbf{z}} \quad (4.22a)$$

$$\hat{\varphi} = -\sin\varphi \hat{\mathbf{x}} + \cos\varphi \hat{\mathbf{y}} \quad (4.22b)$$

$$\hat{\mathbf{r}} = \sin\theta \cos\varphi \hat{\mathbf{x}} + \sin\theta \sin\varphi \hat{\mathbf{y}} + \cos\theta \hat{\mathbf{z}}, \quad (4.22c)$$

meaning the $\hat{\theta}$ and $\hat{\varphi}$ components contain the angular dependence of the radiated SHG, while $\hat{\mathbf{r}}$ is the unit vector directed toward the detector at the specified solid angle, Ω. The laser is centered at $\mathbf{r}_0$ and radiating in the z-axis, meaning $\hat{k}_\omega = \hat{\mathbf{z}}$. We will take the electric field to be polarized in an arbitrary $\hat{\mathbf{u}}$ direction and to be a Gaussian mode,

$$\mathbf{E}_\omega = \hat{\mathbf{u}} E_0 \frac{\exp\left[-\frac{x^2+y^2}{w_0^2(1+i\xi)}\right]}{1+i\xi} e^{ik_\omega z}.$$

Because we normalized the incoming total power, we have $E_0 = \sqrt{P}/(n^2{}_\omega b)$, where P is the power detected at the back aperture of the objective. Using the Gaussian mode, we may further specify our expression for angular SHG to

$$\mathbf{E}_{2\omega}(\Omega, \mathbf{r}_0) = \left[\hat{\theta}, \hat{\phi}\right] \cdot \frac{\omega^2}{c^2} \frac{e^{ik_{2\omega}R}}{4\pi R} \sum_{jk} \hat{\mathbf{x}}_j \cdot \hat{\mathbf{u}}\, \hat{\mathbf{x}}_k \cdot \hat{\mathbf{u}} \int \chi^{(2)}(\mathbf{r}') \times$$

$$\frac{\mathcal{P}}{\omega} \propto \int \frac{n^2 b \exp\left[-2\frac{}{w^2\,(1+2i(z-z\ )/b)}\right]}{(x-x\ )^2+(y-y\ )^2} \frac{\hat{\mathbf{r}}}{(1+2i(z-z\ )/b)^2}\, d\mathbf{r}' \quad e^{i2k_\omega(z-z_0)-ik_{2\omega}\mathbf{r}'\cdot}$$

, (4.23)

where $\mathbf{x}\hat{}_j \cdot \mathbf{u}\hat{}$ is the projection of the polarization vector onto the various Cartesian unit vectors.

From this point on, we will assume the incoming light is purely polarized in $\mathbf{x}\hat{}$ and perpendicular to the long axis of the myosin fibers. This means there is only one nonzero tensor component, χ_{yxx}, so the output light is $\mathbf{y}\hat{}$ polarized, which leads the $\hat{\theta}$ and $\hat{\varphi}$ components to be proportional to $\cos\theta \sin\varphi$ and $\cos\varphi$, respectively. The power per unit solid angle will be proportional to $(\cos^2\theta \sin^2\varphi + \cos^2\varphi)|^R \cdots|^2$, and the total power detected is found by integrating the power density over all φ and the range of θ which is contained within the condenser optic's acceptance angle, namely $\theta_{max} \sim \sin^{-1}(0.55/1.4) \sim 20^\circ$.[5]

Although eq. (4.23) may be integrated directly, for some geometries it is more convenient to work in the conjugate space. Consider the Fourier transform pair of $\chi(x)$:

$$\chi^{(2)}(\mathbf{q}) = \int \tilde{\chi}^{(2)}(\mathbf{r}) e^{-i\mathbf{q}\cdot\mathbf{r}}\, d\mathbf{r}$$

[5] The condenser has a numerical aperture of 0.55. Numerical aperture is defined as $NA = n\sin\theta$, where n is the refractive index of the immersion medium (air for the condenser). The SHG originates

$$\chi^{(2)}(\mathbf{r}) = \frac{1}{(2\pi)^3}\int \tilde{\chi}^{(2)}(\mathbf{q})e^{i\mathbf{q}\cdot\mathbf{r}}\,d\mathbf{q}.$$

Substituting the latter expression into eq. (4.23) gives the relation

$$\mathbf{E}^{2\omega}(\Omega,\mathbf{r}_0) \propto [\cos\theta\sin\phi,\cos\phi]\cdot\frac{\omega^2}{c^2}\chi_{yxx}\iint \tilde{\chi}^{(2)}(\mathbf{q})\times \frac{1}{n^2 b}\exp\left[-2\frac{(x-x_0)^2+(y-y_0)^2}{w_0^2\,(1+2i(z-z_0)/b)}\right]\frac{e^{i2k_\omega(z-z_0)}}{(1+2i(z-z_0)/b)^2}e^{-i(k_{2\omega}\hat{\mathbf{r}}-\mathbf{q})\cdot\mathbf{r}'}\,d\mathbf{r}'\,d\mathbf{q}, \tag{4.24}$$

where we have dropped factors that will not contribute any wavelength dependence.

Having interchanged the order of integrals, we see the spatial integral is equivalent to a Fourier transform of the incoming Gaussian waveform, given by

$$\begin{aligned}\int \frac{1}{n_\omega^2 b}\exp\left[-2\frac{(x-x_0)^2+(y-y_0)^2}{w_0^2\,(1+2i(z-z_0)/b)}\right]\frac{e^{i2k_\omega(z-z_0)}}{(1+2i(z-z_0)/b)^2}e^{-i(k_{2\omega}\hat{\mathbf{r}}-\mathbf{q})\cdot\mathbf{r}'}\,d\mathbf{r}' \\ = \int \frac{1}{n_\omega^2 b}\exp\left[-2\frac{s_x^2+s_y^2}{w_0^2\,(1+2is_z/b)}\right]\frac{e^{i2k_\omega s_z}}{(1+2is_z/b)^2}e^{-i\mathbf{Q}\cdot\mathbf{r_0}}e^{-i\mathbf{Q}\cdot\mathbf{s}}d\mathbf{s} \\ = \frac{\pi^2}{2}\frac{b}{n_\omega^2 k_\omega}e^{-\frac{1}{2}b(Q_z+2k_\omega)}\Theta\left[Q_z-\frac{Q_x^2+Q_y^2-8k_\omega^2}{4k_\omega}\right]e^{-i\mathbf{Q}\cdot\mathbf{r_0}},\end{aligned} \tag{4.25}$$

within the fish muscle, with a refractive index of 1.4. The boundary between muscle/agarose and air will cause the outgoing light to be further bent, so we need to calculate the angle of emission in the agarose corresponding to the maximum acceptance angle in air. Therefore, Snell's law gives $n_{agar}\sin\theta_{max} = n_{air}\sin\theta = NA$, and, thus we have $\theta_{max} = \sin^{-1}(0.55/1.4)$. Because the refractive index is wavelength dependent, θ_{max} will also have wavelength dependence.

where $\mathbf{Q} = k_{2\omega}\hat{\mathbf{r}}-\mathbf{q}$, and $\Theta[\cdot]$ is the unit-step function, $\Theta(x) = \int_{-\infty}^{x}\delta(u)du$. Expanding, we get

$$= \frac{\pi^2}{2}\frac{b}{n_\omega^2 k_\omega}\exp\left[-\frac{1}{2}b(2k_\omega - k_{2\omega}\cos\theta + q_z)\right.$$

$$+i(r_{0z}(q_z - k_{2\omega}\cos\theta) + r_{0x}(q_x - k_{2\omega}\cos\phi\sin\theta) + r_{0y}(q_y - k_{2\omega}\sin\phi\sin\theta))] \times$$
$$\Theta\left[-q_z + k_{2\omega}\cos\theta + \frac{-8k_\omega^2 + (q_x - k_{2\omega}\cos\phi\sin\theta)^2 + (q_y - k_{2\omega}\sin\phi\sin\theta)^2}{4k_\omega}\right] \tag{4.26}$$

which we will abbreviate as $\tilde{G}(\mathbf{q},\mathbf{r}_0,\Omega)$. The outgoing electric field can now be written as

$$\mathbf{E}^{2\omega}(\Omega,\mathbf{r}_0) = [\cos\theta\sin\phi, \cos\phi]\cdot\frac{\omega^2}{c^2}\chi_{yxx}\int\tilde{\chi}^{(2)}(\mathbf{q})\tilde{\mathcal{G}}(\mathbf{q},\mathbf{r}_0,\Omega)\,d\mathbf{q} \tag{4.27}$$

We see that phase-matching is still vital, but the conditions have relaxed, because there is an overall prefactor of $\exp[-\frac{1}{2}b(2k_\omega - k_{2\omega}\cos\theta)]$, shown in eq. (4.26). There may be outgoing directions which provide satisfactory conditions if conventional forward propagation of SHG is poorly matched. This result also explains a common observation of conical radiation in SHG radiation

Myofibrils are very long compared to the focal width of the Gaussian beam, so we can take them to be effectively infinite in extent in the y-direction. In addition, muscles consist of many repeating units. For example, myofibrils are packed full of myosin filaments in a hexagonal fashion. If we take each filament to be a cylinder of radius r_0, denoted as $\Theta(r_0^2 - x^2 - z^2)$, then the entire filament would be a sum of these cylinders, given by

$$\chi^{(2)}(\mathbf{r}) = \sum_{mn}\Theta(r_0^2 - (x - \Delta x_{mn})^2 - (z - \Delta z_{mn})^2) \tag{4.28}$$

and the corresponding Fourier transform[6] is

$$\tilde{\chi}^{(2)}(\mathbf{q}) = 2\pi r_0 \delta(q_y) \frac{J_1(r_0\sqrt{q_x^2+q_z^2})}{\sqrt{q_x^2+q_y^2}} \sum_{mn} e^{-i(\Delta x_{mn} q_x + \Delta z_{mn} q_z)}, \quad (4.29)$$

which reduces to $\tilde{\chi}^{(2)}(\mathbf{q}) = 2\pi r_0 \delta(q_y) \frac{J_1(r_0\sqrt{q_x^2+q_z^2})}{\sqrt{q_x^2+q_y^2}}$ for a single filament. From above, we know $\Delta x_{mn} = n\frac{\sqrt{3}}{2}a$ and $\Delta z_{mn} = (m - n/2)a$.

4.3 Explaining Patterns in Muscle Structure

Second harmonic generation is fundamentally different from fluorescence due to the phase coherence in the harmonic beam, while fluorescent light is incoherent. This primarily influences the radiation direction of second harmonic generation, compared to the isotropic emission in fluorescence. For example, figure 3.3 shows epi-collected fluorescence, i.e.,returning toward the laser source, versus second harmonic, which radiates almost entirely in trans, i.e.,in the same direction as the laser. This phase coherence has additional impact on imaging. Fluorescent signal scales linearly with the number of excited fluorescent molecules in the focus. In contrast, second harmonic generation scales as the square of the number of phase-coherent SHG sources in the focus, and SHG produced away from the focus adds

[6] Due to the cylindrical symmetry of the geometry, this type of transform is often referred to as a Hankel transform instead of a Fourier transform.

coherently to the signal in focus.[7] This phase coherence leads to two prominent motifs in muscle SHG images, as described in section 3.3.1. First, there are the discrete dots, as in figure 3.14. Second, there are the "verniers," or herringbone patterns, as in figure 3.16 and readily apparent in figure 3.18, although they common in almost every image.

To investigate, we first consider a numerical simulation of the SHG microscopy. Consider a numeric map of the susceptibility, simplified for the purposes of the calculation, given by $M(x,z)$, where $\hat{z}$ is the direction of propagation. The value taken on by $M(x,z)$ denotes a effective scalar susceptibility, either 1, 0, or -1 [113]. To construct a hypothetical muscle, we map out myofibrils as discrete rectangles of myosin, whose size and shape mirror the A-bands of sarcomeres. The myosin blocks are arranged in rows, representing myofibrils, depicted in figure 4.3(a). Because myosin thick filaments project from the M-line, which is at the center of the sarcomere, each half sarcomere has oppositely signed susceptibilities,[8] represented by the different colors in figure 4.3(a). The hypothetical myofibrils are arranged in parallel and in phase, building up a myocyte. A second myocyte, placed 180 $^\circ$ out of phase is constructed adjacent to the first.

[7] This may have a significant impact on SHG confocal microscopy, because signal produced away from the focus propagates in a Gaussian mode with an identical focus as the fundamental beam, and cannot be excluded with a pinhole. Thus, the success of SHG confocal microscopy is likely explained by the fact that light is fundamentally quantized, and, for biological samples, SHG efficiency drops off sufficiently away from the focus that zero photons are produced.

[8] A fundamental property of second-order nonlinear susceptibility is inversion due to change of parity: $\chi^{(2)}(-x) = -\chi^{(2)}(x)$. If the underlying material possess inversion symmetry, such as at the M-line, we must have $\chi^{(2)} = 0$.

More specifically, let $Sq(x,d)$ be a square wave with period 2π and duty cycle d%, then if $\Delta z < z < \Delta z + w_s$, where $\Delta z = 0.1\ \mu$m is the spacing between sarcomeres

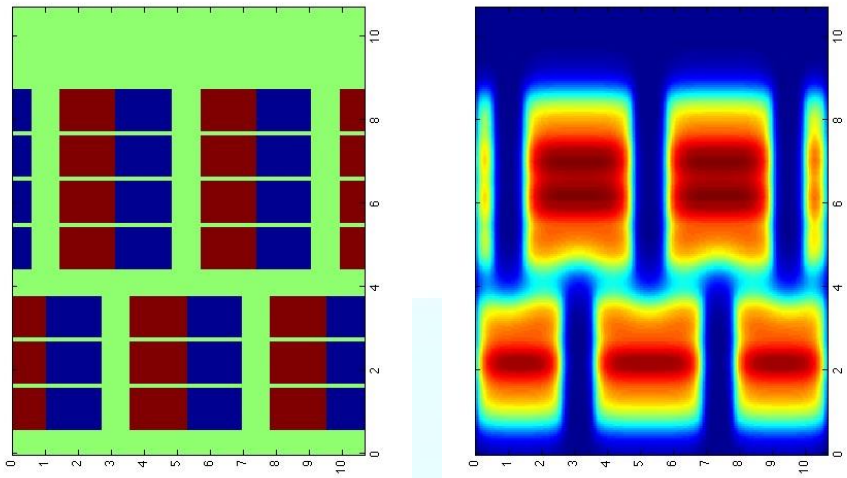

(a) Scheme of two adjacent myofibrils. (b) two-photon fluorescence from Only myosin is shown. Color indicates myosin.
the chirality of the myosin filaments, and the
boundary between them is the
M-line.

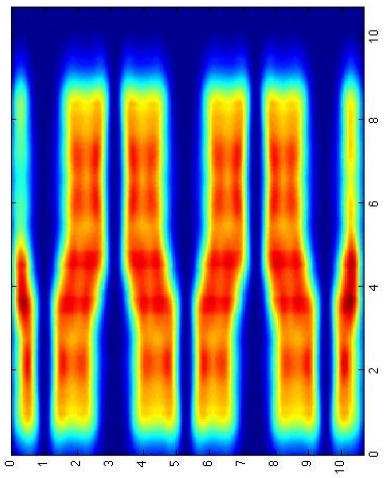

(c) SHG from myosin.

Figure 4.3: Theoretical calculations illustrate the qualitative difference between SHG and two-photon fluorescence. Two hypothetical myofibrils touch, one slightly out of phase with the other. If the myosin were labeled with a fluorescent dye, one would measure discrete points of light, with little or no signal joining the myofibrils. However, the coherent nature of SHG causes the appearance of a contiguous, single myofibril, with a "vernier." In these images, the laser comes propagates vertically, corresponding to an image such as figure 3.18.

and $w_s = 1\ \mu$m is the width of the sarcomere,

$$M(x,z) = \max[Sq(2\pi x/p,d),0]Sq(2\pi x/p,d/2), \tag{4.30}$$

where $p = 5\ \mu$m is the length of the sarcomere, and $d = 80\%$. This maps out the susceptibility of a single myocyte, as in figure 4.3(a), assigning each point a susceptibility of 1, -1, or 0. For the second set of fibrils, a phase factor of π is added.

Many biological experiments use fluorescent stains, so we calculate what would be observed if the muscle represented by $M(x,z)$ were imaged using a two photon microscope. The incoming beam is a Gaussian, given by

$$E(x,z) = \frac{\exp\left[-\frac{x^2}{w_0^2(1+i\xi)}\right]}{1+i\xi} e^{ik_\omega z}, \tag{4.31}$$

where w_0, Δk, and ξ are the focal radius, phase mismatch, and normalized Rayleigh distance, as defined in section 4.2.1, evaluated using $\lambda = 0.850\ \mu$m and NA= 0.8. To construct the image, the absolute value of eq. (4.31) is squared and then convolved with the absolute value of $M(x,z)$. The square of this result is proportional to the intensity of fluorescence incident on the detector, and is pictured in figure 4.3(b).

To calculate the SHG produced by this image, we employ the Green's function approach, taken from eq. (4.23). In this case, we only care about the field collected by the detector, so, for an incoming Gaussian, the effective Green's function for SHG on-axis ($\theta = 0$) is

$$E(x,z) = \frac{\exp\left[-2\frac{x^2}{w_0^2(1+i\xi)} + i\Delta kz\right]}{(1+i\xi)^2}, \tag{4.32}$$

where the parameters are determined in the previous two-photon case. The Green's function is convolved with $M(x,z)$. The absolute value of the result squared gives the intensity of the SHG produced at each point, shown in figure 4.3(c). Notice that SHG is detected from the regions free of any myosin. This is due to the Gouy phase of the laser, where the phase of light switches by π through the focus. Because the neighboring fibers are out of phase by π, the combination with the Gouy phase produces constructive interference when the focus of the laser is between two fibers. A close look at figure 4.3(c) will reveal bright nodes within the SHG stripes, corresponding to the dots in figure 3.14 which appear when imaging through a sagittal plane.

Comparison with the image of $M(x,z)$, in Fig 4.3(a). will show that no SHG originates from from the M-line, the boundary between $M = 1$ and $M = -1$ in our simulation. This is due to the inversion symmetry where the myosin fibers project in opposite directions. This results in the appearance of doublets in the SHG image, two bright points for each sarcomere. When the sarcomere contracts, some authors

observe that the doublets are replaced by a single wide bright spot [105, 101]. One explanation is that uneven contractile forces disrupt the boundary at the M-line [100]. Although this explanation may be correct, our simulations show that the doublet disappearance may simply be due to the fibers rotating in and out of plane. Adjusting the laser angle in the simulation by less than 20° causes the doublets to disappear, replicating what appears to be observed in experiments, as in figure 4.4(d). Symmetry at the M-line only exists with respect to the inversion along the axis of the sarcomere. When the laser is perpendicular to the axis of the sarcomere, one observes the doublets. Once out of alignment, the Gouy phase of the laser causes constructive interference between the myosin on either side M-line, and SHG is observed where none was before.[9] Contraction increases this effect, because sarcomeric volume conservation [93, 96] increases the width of the sarcomere, giving the laser more myosin to interact with, shown in figure 4.4.

The effects demonstrated here arise from the coherence of SHG, demonstrating how the specific spatial arrangement of SHG-active material can enhance or quench the resulting SHG. Because the focusing properties, refractive index, and phasematching are wavelength dependent, we also anticipate that coherence will produce a spectral signature specific to the underlying crystallinity of the SHG media.

[9] In fact, Plotnikov et al. observe "[When the myofibril contracts,] some changes of SHG intensity were observed at ends of myofibrils that moved out of the plane of section." [101] Thus, it appears it would not be unusual for a dynamic fibril to squirm out of alignment by a few degrees and cause the doublets to disappear.

4.4 Wavelength Dependence of SHG

To understand the wavelength dependent SHG spectra measured in Figs. 3.21 and 3.23, we have to account for possible sources of wavelength dependence. As described in section 3.2, the data was corrected to remove instrument-dependent wavelength sensitivities. This leaves phase-matching and the nonlinear susceptibility, $\chi^{(2)}(\omega)$, as sources of dispersion. As with the index of refraction, the nonlinear susceptibility will be far from any resonances. Away from absorption resonance, the wavelength dependent portion of the susceptibility may be expressed in terms of first-order optical

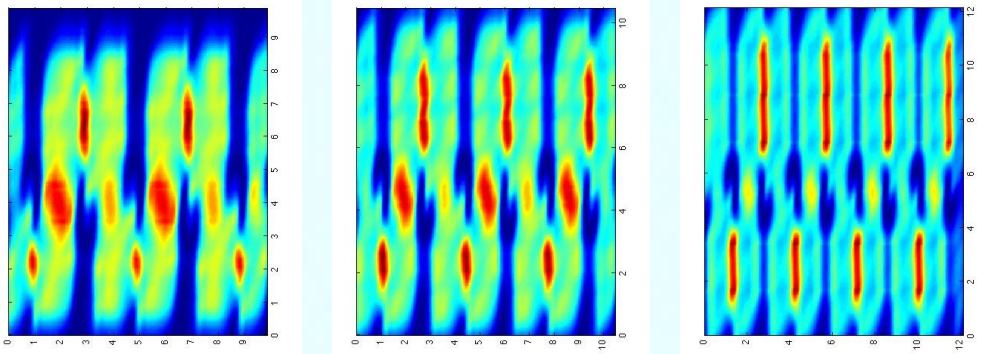

(a) 5 μm sarcomere (b) 4 μm sarcomere (c) 3 μm sarcomere

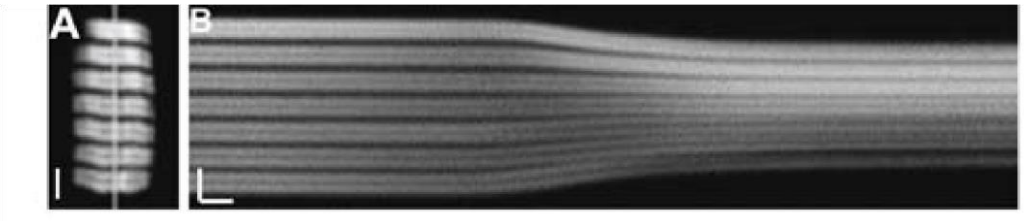

(d) Experiment [101]

Figure 4.4: Using the same schematic as figure 4.3(a), when the laser is tilted by 20 $^\circ$, the doublets disappear. (a)-(c) When accompanied by contracting sarcomeres, the effect is even more pronounced. (d) Compare to the experimentally observed time lapse of a contracting myofibril, adapted from [101]. A snapshot of the myofibril is labeled A (scale bar 2.5 μm, and a space-time diagram of the recorded contraction is labeled B (vertical scale, 2.5 μm; horizontal scale, 0.5 s). Note that the experimental image is in a perpendicular plane to the simulation.

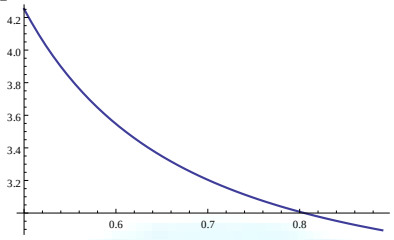

Figure 4.5: The nonlinear susceptibility of muscle, $\chi^{(2)}(\omega)$, based on Miller's rule.

properties using Miller's rule [148, 149, 150]:

$$\chi^{(2)}(\omega) \propto \chi^{(1)}(2\omega)\chi^{(1)}(\omega)^2$$
$$\propto (n_{2\omega}^2 - 1)(n_{\omega}^2 - 1)^2. \quad (4.33)$$

Because the refractive index decreases monotonically with increasing wavelength, the SHG susceptibility monotonically decreases with wavelength (or increases with frequency) in the wavelength range of concern, as plotted in figure 4.5. It does not contain the steep drop-off observed in the experimental data. This leaves phasematching as the remaining factor to explain Figs. 3.21 and 3.23.

If we treat the entire muscle as a uniform block of amorphous SHG-active material, we would find the spectrum would vary with depth [151, 67, 141]. Similarly, we would also expect the intensity to vary significantly with depth [71]. Neither is

observed.[10] Instead, the spectrum is nearly uniform from edge to edge, as is the intensity, up to the expected effects of field attenuation (see figure 3.8). This implies that the SHG is originating only from the focus. In two-photon fluorescence microscopy, this is an advertised feature, but numerous experiments have demonstrated significant SHG production away from the focus in phase-matched crystals [152, 139]. Although the effective production of SHG would be limited to the focus if the SHG were to produced noncollinearly (i.e.,with some walk-off angle due to birefringence), walk-off angles tend to be very small – only a few degrees [153, 111], which for our optical setup would be of little consequence compared to the size of the focus.[11] Two possible explanations remain: the quasi-crystalline nature of the muscle fibers on either side of the focus can cause the SHG to pick up phase errors, reducing the effective phasematching [154], making SHG coherent only near the focus. Or, the SHG efficiency is so low that photons are only produced near the focus.

I have taken two approaches to using theory to understand the wavelength dependence. First, to calculate the SHG conversion, we combine quasi-phase-matching with a focused Gaussian beam. This approach requires guessing at the underlying superstructure of the muscle fibers, and it provides us with an insight into hidden correlation length-scales. Second, using the Green's function approach, we

[10] I'm not saying such a dependence does not exist, just that other SHG efficiency-altering factors prevent observing any systematic variation of this type.

[11] The effective aperture length for SHG production due to walk-off is $\ell_a = \sqrt{\pi w_0/\rho}$, while the effective length of the focus is $\ell_f = \pi b/2 = \pi k w_0^2/2$ [152]. Thus, walk-off will limit SHG production if $\ell_f/\ell_a = \pi^{3/2} n w_0 \rho/\lambda = \pi^{1/2}\rho/\mathrm{NA} > 1$. NA = 0.8, so walk-off will not be an issue for $\rho \sim 1$ degree (0.02 radians), which is a generous estimate for the spatial walk-off angle for muscle.

calculate the contribution of the wavelength dependence due to changes in collection efficiency.

4.4.1 Wavelength Dependence Due to Myofibril Packing

Under the paraxial approximation, the SHG conversion due to periodic packing of myofibrils is given by

$$F(\Delta k, z_0, z_f) = \int_{z_0}^{z_f} \sum_{mn} G_{mn} \frac{\exp\left[i(\Delta k z + K_{mn} z)\right]}{1 + i\xi}\, dz, \tag{4.34}$$

where the focus of the laser is at $z = 0$, and z_0 and z_f are the boundaries of the SHG active area. The laser passes through many layers of sarcomeres as it images, and these layers are arranged in a quasi-crystalline manner. The fibers are arranged in a multitude of orientations, states of contraction (sarcomere length), and relative alignment. Thus, the final value results must not be so sensitive to these parameters as to only apply in unrealistically rigid conditions. Because of the drop-off around 850 nm is due to phase-matching, we can interpret the spectra to be reporting some sort of quasi-phase-matching which is only effective up to 850 nm. Thus, we consider the critical lengths created by the phase mismatch, $`_c = |\lambda/(2(n_{2\omega} - n_{\omega}))|$, plotted in figure 4.7. The better the phase-matching, the longer the critical length, but the only truly predictable length scale is the sarcomere length, which is around 2-3 μm. However, the randomness of the orientations mean there will be some effective length that can be used as a fitting parameter.

The structure of muscle was represented using a 1-D function to mimic the density

of sarcomeres,

$$M(z,p) = ((4 - \sin[\pi\frac{z}{2p}]^4 \cos[\pi\frac{z}{p}]4(1 + \cos[2\pi\frac{z}{p}])^2)/2)^4, \tag{4.35}$$

which produces a periodic structure of finite bandwidth, diagrammed in figure 4.6(a). To create a spatial map of the susceptibility, $\chi^{(2)}{}_M$, $M(x,p)$ is transformed with a square wave with half of the period,

$$\chi_M^{(2)} = M(z,p)Sq(2\frac{x}{p}), \tag{4.36}$$

which is shown in figure 4.6(b). Instead of decomposing $\chi_M^{(2)}$ into its inherent Fourier components, integration was carried out directly. That is,

$$F(\Delta k, z_0, z_f) = \int_{z_0}^{z_f} \chi_M^{(2)}(z,p)\frac{\exp[i\Delta kz]}{1 + i\xi}\, dz. \tag{4.37}$$

To fully account for wavelength dependence, we include the wavelength dependence of the power density (eq. (4.7)) and susceptibility (eq. (4.33)), and fitted p to the representative spectra in figure 3.21(c) and taking $z_0 = -100$, $z_f = 100$ μm.

The resulting fit is shown in figure 4.8. The fit produced p = 5, approximately the same as the alignment of bundles of myofibrils, as seen in figure 3.20. Although 5 μm is a bit too large for ordinary sarcomeric structure, it suggests a stronger intermyofibril alignment. Further experiments on isolated myofibrils will be essential to separate any further wavelength dependence not due to myofibril alignment. The

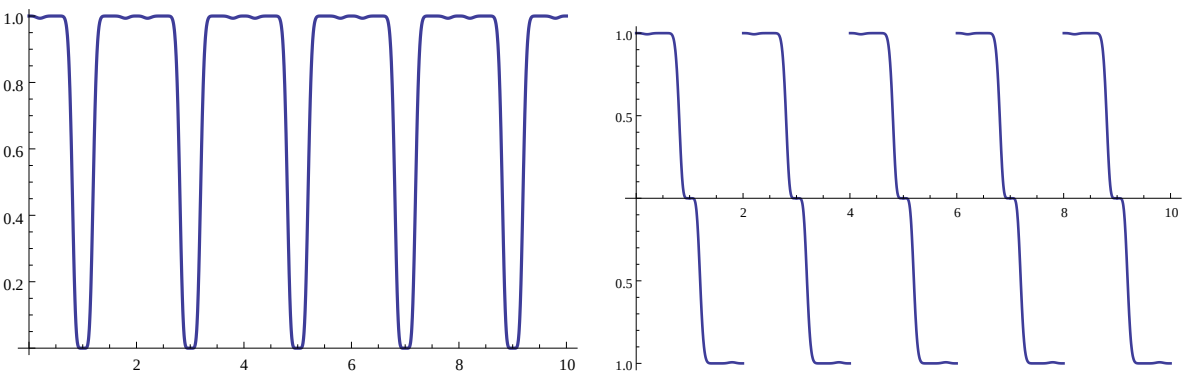

(a) $M(x,p = 1)$ (b) $\chi_M^{(2)}(x, p = 1)$

Figure 4.6: Plot of SHG susceptibility map. Here, $p = 2$.

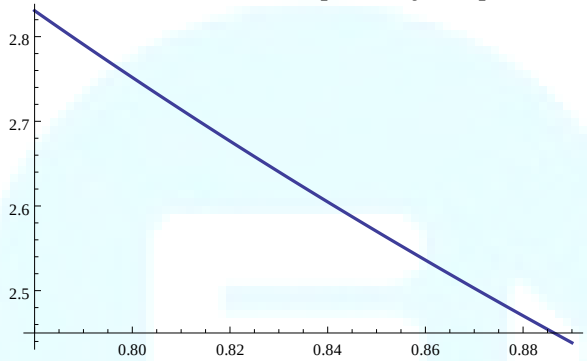

Figure 4.7: $\grave{}_c$ as a function of wavelength for the refractive index defined in Eq 3.1. All units are μm.

fit required the use of an experimentally observed refractive index that was larger concave down, instead of more commonly observed concave up shape [79]. Although myofibrils are highly aligned with the immediate neighbors, visual inspection (such as figure 3.17(a)) show there is a scale of structure between a full myocyte and a single myofibril. This work suggests that a length scale of 5 μm appears to be an as yet uncharacterized length-scale of importance within zebrafish muscle.

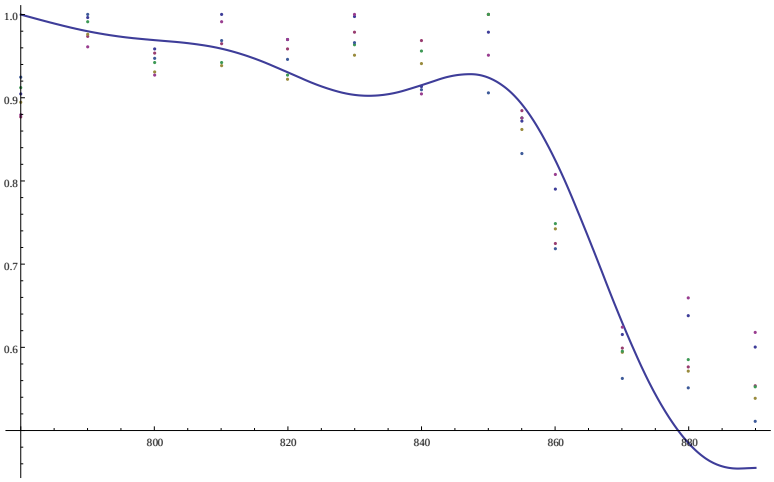

Figure 4.8: Fit of eq. (4.37) using the quasi-phase-matching structure in eq. (4.36), with p = 5 μm. The experimental data are from figure 3.21. The x-axis is wavelength in nanometers, and the y-axis normalized intensity.

4.4.2 Wavelength Dependence Due to Collection Efficiency

As stated in section 4.2.2, only SHG emitted with in a limited angular cone will be detected. The cutoff angle is given by $\theta_{\max} = \sin^{-1}(0.55/n_{2\omega})$. Because the cutoff angle varies with wavelength, we expect the collection efficiency to systematically vary. The SHG emission angles also vary with wavelength, as shown in figure 4.9, and this will contribute as well.

The energy detected by the microscope is given by

$$I(\lambda, \mathbf{r}_0) \propto \int_0^{\theta_{\max}(\lambda)} d\theta \int_0^{2\pi} d\phi \mathbf{E}^*_{2\omega}(\Omega, \mathbf{r}_0)\mathbf{E}_{2\omega}(\Omega, \mathbf{r}_0), \tag{4.38}$$

where $\mathbf{E}_{2\omega}(\Omega,\mathbf{r}_0)$ is given by eq. (4.27). Because light is quantized, SHG photons only appear, statistically, from a limited region around the focus. The size of this region depends on the wavelength of light and the intensity of the incoming laser. Using a

Green's function approach to calculating the emitted SHG, we find the wavelength

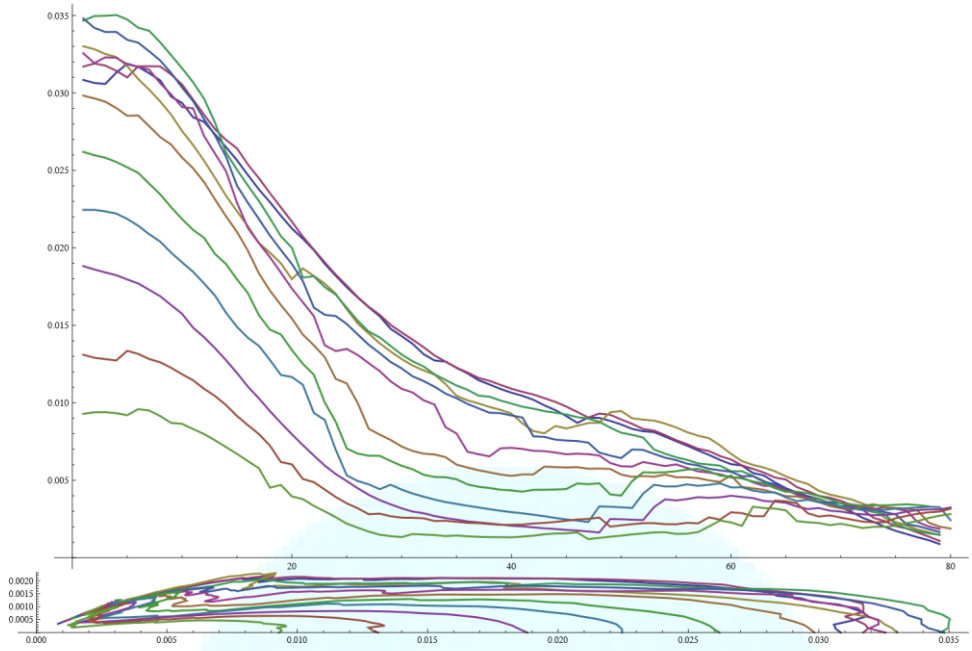

Figure 4.9: SHG emission intensity is angle dependent. (top) SHG intensity as a function of emission angle, the degrees. (bottom) Polar plot of SHG emission. Input wavelength varies from 790 nm to 890 nm, ordered from the bottom up. This plot is not corrected for other wavelength dependent factors. Each curve ends at the maximum angle for collection.

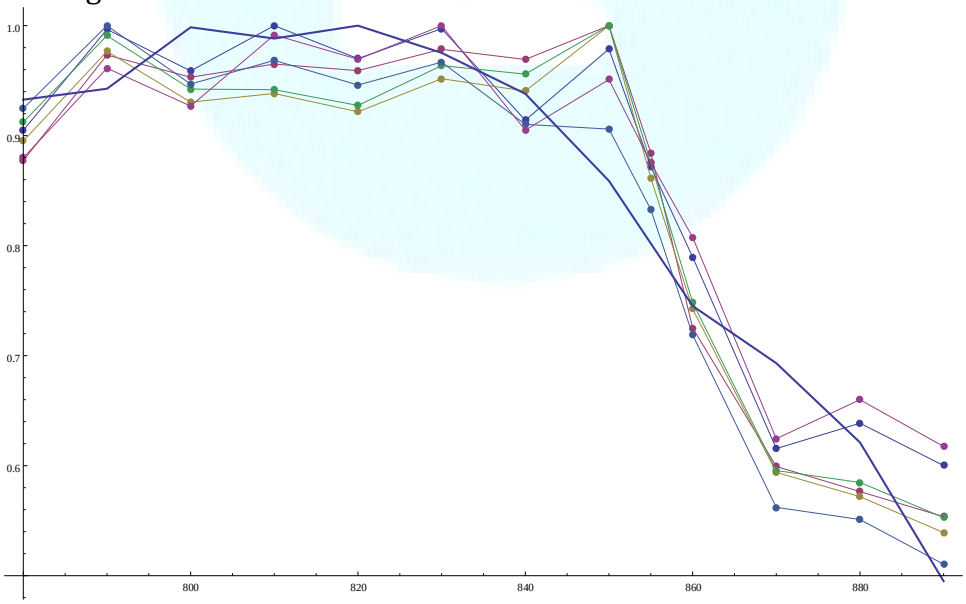

Figure 4.10: The wavelength dependent SHG may also be due to the variation of the size of the laser focus. Here, the SHG active region was constrained to a box extending $5.2b$ along the z-axis and $1.9w_0$ along the x- and y-axis.

dependent intensity aligns well with the data, shown in figure 4.10.

The collection efficiency has a noticeable effect on SHG production from a myocyte. By calculating how collection efficiency and the size of the SHG production volume vary with wavelength, we show the promise of the Green's function approach to capture effects that are beyond the reach of the paraxial approximation. Further work, such as varying the laser intensity to alter the size of the SHG production volume, will allow the Green's function approach to refine our conclusion from the previous section, which were based on the paraxial approximation. Because the kink occurs around 850 nm, we can reasonably hypothesize that part of the effect we see in the wavelength dependence of the SHG from zebrafish myosin is due to wavelength dependent collection efficiency.

4.5 Conclusion

Through the last two chapters, we have experimentally and theoretically analyzed the nonlinear optical properties of zebrafish muscle. Although other works have done an excellent job characterizing the susceptibility of myosin, none has considered the wavelength dependence or closely examined how SHG images differ from fluorescence images. We have determined that the crystalline structure of muscle fibers alters the wavelength dependence away from the inherent susceptibility of an isolated myosin protein. This informs us about the underlying packing of the myocytes. Future experiments which capture not just the intensity of the resulting SHG but also the spatial dependence of the far-field SHG radiation pattern will permit

full inversion to find the underlying structural detail. For now, we inferred our results by fitting the data to a hypothetical myocyte.

By calculating the expected patterns produced from the highly structured packing of sarcomeres, we have provided some surprising results, such as explaining the disappearance of the doublets and origin of the herringbone pattern lines as not necessarily being biological in origin, but a fundamental feature of coherent SHG imaging. Because SHG is a coherent process, it produces microscopy images that require closer consideration than fluorescence. With fluorescence, the intensity of a pixel is proportional to the amount of dye in the focal volume, but with SHG, as the present results show, the intensity of a pixel is not a nontrivial correspondence to the microscopic arrangement of SHG susceptible material.

Further work, such as studying a single myofibril, comparing the SHG from different organisms, and repeating a similar analysis on collagen, will help to confirm the predictions made here. Time resolved imaging of muscle development may cast further light onto newly identified organized length scale of 5 μm. More detailed calculation, made without the strong assumptions implicit in the paraxial approximation, will also allow further refinement of our interpretations of the SHG images produced here.